The global melt inclusion C/Ba array: mantle variability, melting process, or degassing?

Simon Matthews[a,*], Oliver Shorttle[a,b], John Maclennan[a], John F. Rudge[a]

[a] *Department of Earth Sciences, University of Cambridge, Downing Street, Cambridge, CB2 3EQ, UK.*
[b] *Institute of Astronomy, University of Cambridge, Madingley Road, Cambridge, CB3 0HA, UK.*

Abstract

The Earth's mantle holds more carbon than its oceans, atmosphere and continents combined, yet the distribution of carbon within the mantle remains uncertain. Our best constraints on the distribution of carbon within the upper mantle are derived from the carbon-trace element systematics of ultra-depleted glasses and melt inclusions from mid-ocean ridge basalts. However, carbon-trace element systematics are susceptible to modification by crustal processes, including concurrent degassing and mixing, and melt inclusion decrepitation. In this study we explore how the influence of these processes varies systematically with both the mantle source and melting process, thereby modulating both global and local carbon-trace element trends.

We supplement the existing melt inclusion data from Iceland with four new datasets, significantly enhancing the spatial and geochemical coverage of melt inclusion datasets from the island. Within the combined Iceland dataset there is significant variation in melt inclusion C/Ba ratio, which

*Now at Institute of Earth Sciences, University of Iceland, Sturlugata 7, 101 Reykjavik, Iceland. simonm@hi.is

is tightly correlated with trace element enrichment. The trends in C/Ba-Ba space displayed by our new data coincide with the same trends in data compiled from global ocean islands and mid-ocean ridges, forming a global array. The overall structure of the global C/Ba-Ba array is not a property of the source, instead it is controlled by CO_2 vapour loss pre- and post-melt inclusion entrapment; i.e., the array is a consequence of degassing creating near-constant maximum melt-inclusion carbon contents over many orders of magnitude of Ba concentration.

On Iceland, extremely high C/Ba (>100) and C/Nb (>1000) ratios are found in melt inclusions from the most depleted eruptions. The high C/Ba and C/Nb ratios are unlikely to be either analytical artefacts, or to be the product of extreme fractionation of the most incompatible elements during silicate melting. Whilst high C/Ba and C/Nb ratios could be generated by regassing of melt inclusions by CO_2 vapour, or by mantle melting occurring in the presence of residual graphite, we suggest the high values most likely derive from an intrinsically high C/Ba and C/Nb mantle component that makes up a small fraction of the Icelandic mantle.

Keywords: Mantle, Carbon, Heterogeneity, Iceland, Melt Inclusions, Decrepitation

---

1. Introduction

Carbon fluxes in-to and out-of the mantle regulate Earth's carbon cycle on geological timescales (Lee et al., 2019). Chemical mass-transfer between the Earth's interior and exterior is achieved by melt-extraction and subduction of oceanic lithosphere. Whilst there is good experimental (Rosenthal

et al., 2015) and empirical (Saal et al., 2002; Matthews et al., 2017) evidence that carbon is removed efficiently from the mantle by melt-extraction, the efficiency with which carbon is returned to the deep mantle remains unclear. Thermodynamic modelling suggests most carbon in subducting slabs will be removed during slab dehydration (Kelemen and Manning, 2015); however, the flux of carbon into subduction zones is substantially greater than the flux of carbon out of arc volcanoes (Aiuppa et al., 2019; Plank and Manning, 2019). This missing carbon might be trapped in the lithospheric mantle beneath volcanic arcs (Kelemen and Manning, 2015), or it could be returned to the convecting mantle (Hirschmann, 2018).

Recycling of oceanic lithosphere throughout geological time is recorded in the substantial small-scale mantle heterogeneity it creates. The geochemical signal of recycled heterogeneities is particularly prevalent in ocean island basalts (OIB), the product of melting within deeply-derived mantle plumes (e.g., Hofmann, 1997). If significant quantities of carbon are returned to the deep mantle by subducted lithosphere, the mantle's carbon concentration ought to display equivalent small-scale heterogeneity. Whilst a number of studies have suggested that mantle plumes are carbon rich (Trull et al., 1993; Anderson and Poland, 2017; Boudoire et al., 2018; Tucker et al., 2019), and that high ^{3}He mantle domains have high CO_2 (Miller et al., 2019), small-scale heterogeneity associated definitively with recycled carbon is yet to be demonstrated.

Basaltic lavas are our most direct probe of the chemistry of the convecting mantle and its heterogeneity (e.g., White, 2015). Progress in identifying mantle carbon heterogeneity has been hampered by its tendency to exsolve

from magmas into a CO_2 vapour phase. The solubility of CO_2 in basaltic melts is minimal at the low pressures of eruption (Stolper and Holloway, 1988), with the consequence that considerable carbon will have been lost from the melt by CO_2 vapour exsolution (degassing) in all but the most carbon-poor melts. Magmas that sample recycled mantle components tend to be enriched in trace elements. If such magmas are similarly enriched in CO_2, they will be more susceptible to degassing processes than magmas sampling depleted mantle components. This interplay of source and process could, therefore, introduce systematic biases in carbon-trace element trends as the contribution to magmas from recycled mantle components increases.

In this contribution we assess the evidence provided by melt inclusions for small-scale carbon heterogeneity in Earth's mantle, both within Iceland and at the global scale.

1.1. Estimating mantle carbon

A number of approaches have been taken to circumvent the overprint of degassing on mantle carbon signals. Rare ultra-depleted glasses erupted in oceanic fracture zones often contain sufficiently low concentrations of carbon that they are undersaturated in CO_2 vapour at the pressure of eruption. However, Matthews et al. (2017) suggested that even these ultra-depleted magmas might not preserve their primary carbon concentrations. In their model, a CO_2 vapour-undersaturated magma can be generated by mixing CO_2 vapour-saturated magmas with extremely C-depleted magmas. This mixing process cannot be definitively identified from the ultra-depleted glass alone; but if it occurs, the carbon concentration in mantle sampled by ultra-depleted glasses is, consequently, underestimated. Occasionally, extremely

trace-element enriched mid-ocean ridge basalt (MORB) glasses retain gas rich vesicles, which may contain the full budget of CO_2 and other volatiles that exsolved from the magma (Cartigny et al., 2008; Jones et al., 2019). It is again unclear whether these enriched magmas lost additional CO_2 vapour deeper within the crust, before beginning to retain vesicles. Furthermore, the MORB glass datasets provide information only about the mantle underlying the mid-ocean ridge system, and are therefore biased towards characterising volumetrically dominant depleted mantle components.

Another approach uses melt inclusions, tiny droplets of magma trapped within crystals as they grow at depth within the crust. The elastic strength of the host crystals prevents decompression of the inclusion to the pressure of the surrounding melt, potentially allowing the trapped melt to remain undersaturated in CO_2 vapour. Not only are melt inclusions often found in MORB, they can be readily found in ocean island basalt (OIB). Melt inclusions also provide an unrivalled view of the earliest stages of magma evolution, when the diversity of melt chemistry generated by near-fractional melting is still partially preserved (Sobolev and Shimizu, 1993). However, the carbon budget of melt inclusions remains susceptible to the same degassing and mixing processes as the ultra-depleted glasses, in addition to carbon partitioning into vapour bubbles in the inclusions (e.g., Métrich and Wallace, 2008; Hartley et al., 2014). Post-entrapment CO_2 vapour loss via decrepitation of the host crystals is also likely to occur (Maclennan, 2017).

1.2. Ratios of carbon and trace-element concentrations

Melting is one process affecting carbon that it may be possible to successfully control for. Ratios of C to Ba, or Nb, concentrations have been

used to achieve this (Saal et al., 2002; Le Voyer et al., 2017; Hauri et al., 2018; Michael and Graham, 2015; Shimizu et al., 2016; Tucker et al., 2019; Shimizu et al., 2019; Miller et al., 2019), since C, Ba, and Nb partition similarly during mantle melting (Saal et al., 2002; Rosenthal et al., 2015). Given the similarity in partitioning behaviour, it should be expected that pre-degassing magmatic values of C/Ba and C/Nb will not be fractionated from their mantle sources; the exception to this being that even small differences between the partition coefficients can cause large variations in the C/Ba and C/Nb of instantaneous fractional melts extracted from a previously depleted source (Rosenthal et al., 2015).

A number of previous studies (Saal et al., 2002; Le Voyer et al., 2017; Hauri et al., 2018) are predicated upon correlations between C and Ba, or Nb, concentrations in melt inclusion suites indicating a lack of any fractionation between carbon and the incompatible trace elements, including the absence of CO_2 vapour degassing prior to, or after, inclusion entrapment. However, Matthews et al. (2017) demonstrated that such correlations are also a natural consequence of degassing and mixing of compositionally diverse near-fractional mantle melts, and such a process can explain the increasing variation in C/Ba ratio with C concentration that many datasets exhibit.

Magma mixing is ubiquitous in magmatic systems (Sobolev, 1996; Maclennan, 2008a; Shorttle, 2015; Shorttle et al., 2016), and the most carbon rich fractional melts are expected to saturate in CO_2 vapour at pressures within, or below, the crust (Dixon et al., 1995). Though the degassing and mixing process causes the average value of C/Ba within a dataset to be controlled primarily by the pressure of degassing, the maximum values seen in a dataset

may still record the mantle value (or are at least a minimum estimate of the mantle value). Datasets that do not exhibit correlations likely have a more complex multi-stage degassing history, making them less reliable records of mantle C/Ba ratios.

Shimizu et al. (2019) recently demonstrated that not all melt inclusion datasets require a partial-degassing and mixing process to explain their carbon–trace element systematics. For inclusions from the Siqueiros and Garrett transform faults, Shimizu et al. (2019) showed that the covariance of carbon concentrations with the concentrations of a broad suite of trace elements is consistent with the trapped melts having a single mantle-derived C/Ba ratio for variable Ba concentration. The observed variability in C/Ba and C/Nb ratios within the data was argued to arise from analytical precision (Shimizu et al., 2019). However, partially degassed datasets can contain melt inclusions with a single C/Ba ratio at variable Ba concentration. If the trace-element and carbon-enriched melts degas, but are then efficiently homogenised, a single enriched mixing endmember is produced, with a C/Ba ratio lower than the mantle value (Matthews et al., 2017, Appendix A). When mixed with extremely trace-element and carbon-depleted melts, a binary mixing array in C-Ba space will be generated with each melt having an identical C/Ba ratio. In this scenario, the mean C/Ba ratio of the datasets would then be only a minimum bound on the mantle value.

Whilst we often treat carbon as if it were a lithophile trace element during mantle melting, like Ba or Nb (Saal et al., 2002; Rosenthal et al., 2015; Matthews et al., 2017), this might not reflect the reality of carbon transfer into melts. Rather than behaving as a passive tracer element, when a

carbon-bearing phase is present, carbonatitic or carbonated-silicate magmas are likely to be the first melts to form (Dasgupta and Hirschmann, 2010). Such small degree melts of the convecting mantle are never observed at the surface, suggesting that they are efficiently mixed with the deepest-forming silicate melts during transport to lower pressures. Regardless of how the first melt forms, the deepest melts that survive transport will contain the majority of the carbon and Ba budget, and retain the mantle C/Ba ratio. Even refractory mantle lithologies are likely to have entirely lost their carbon to a melt phase long before silicate melting begins. Though treating carbon as a trace element during mantle melting is a simplification, it is unlikely to make a meaningful difference to our understanding of carbon-trace element systematics.

1.3. Identifying small-scale mantle carbon heterogeneity

To deconvolve the signals of CO_2 vapour degassing and mantle carbon heterogeneity, a large number of melt inclusions from eruptions sampling a diversity of mantle sources need to be analysed for both their trace element and carbon concentrations. Iceland offers an excellent opportunity for studying carbon heterogeneity within a single mantle plume due to the large number of previous melt inclusion studies (Hauri et al., 2018; Hartley et al., 2014; Neave et al., 2014; Bali et al., 2018; Schipper et al., 2016; Miller et al., 2019), which we supplement with four new datasets (Sections 2 and Section 3).

Comparisons between the carbon-trace element systematics present within the Icelandic melt inclusion compilation and the global compilation enable us to make a new assessment of the effects of crustal storage and melt inclusion

decrepitation (Section 5). Though this secondary crustal processing signal dominates the local and global C/Ba and C/Nb arrays, some datasets preserve C/Ba and C/Nb variability that is not necessarily explained by crustal processing, including extremely high values of C/Ba and C/Nb. In Section 6, we consider the processes that might generate such extreme C/Ba and C/Nb from a source with lower, less extreme, C/Ba and C/Nb. Whilst processes that could fractionate the C/Ba and C/Nb ratios from their source cannot be conclusively ruled out, we argue it is most likely that the datasets do preserve evidence for small-scale mantle heterogeneity in C/Ba and C/Nb. In Section 6.5, we consider the implications of small-scale mantle C/Ba and C/Nb heterogeneity for the presence of small-scale heterogenentiy in mantle carbon concentration, but save a full quantitative analysis for future work.

2. Samples and Methods

Samples were collected from four eruptions of primitive basalt in Iceland (Figure 1a) which represent diverse mantle sources, as indicated by their Sr-, Nd-, and He-isotope ratios (Figure 1b and 1c). Háleyjabunga and Stapafell are in close proximity on the Reykjanes Peninsula in the Western Rift Zone, but preferentially sample more depleted and enriched mantle components respectively (Thirlwall et al., 2004). Stapafell erupted sub-glacially between 70 and 14 ka (Saemundsson et al., 2010) forming basal pillow basalts, from which samples were taken near 63°54.585'N, 22°31.409'W. Háleyjabunga was erupted as a sub-aerial lava shield at ∼13 ka (Saemundsson et al., 2010), from which olivine-phyric lava flow samples were taken from the Eastern side of the vent near 63°48.978'N, 22°39.099'W. Berserkjahraun is an eruption younger

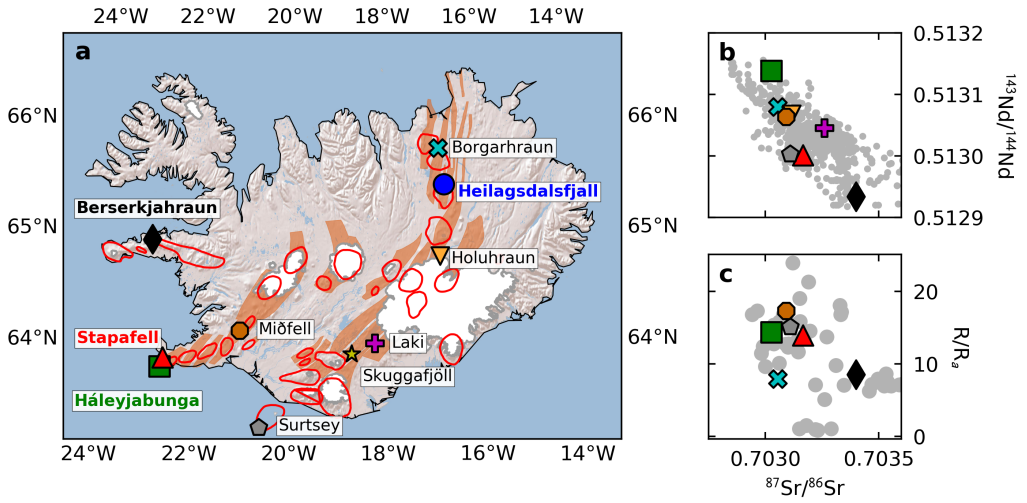

Figure 1: Panel a: Locations of the eruptions studied here (bold text and large symbols), and the locations of other Icelandic eruptions for which carbon and trace element measurements have been made on melt inclusions. Orange shading shows the active rift zones. Red outlines show active volcanic centres. Panel b: Sr and Nd isotope ratios of whole rocks from the same eruptions. Panel c: $^3He/^4He$ isotope ratio (R) normalised to the atmospheric value (R_a). Grey circles in panel b show data compiled for Iceland (sources given in Supplementary Text D). Isotope data not available for Skuggafjöll and Heilagsdalsfjall.

than 11 ka in the Snæfellsnes flank zone (Hjartarson and Sæmundsson, 2014), and has extreme geochemical enrichment (Peate et al., 2010). Glassy olivine- and plagioclase-phyric scoria was collected from the crater at 64°95.915'N, 22°89.853'W. The Heilagsdalsfjall samples were obtained from olivine-phyric tephra erupted from young craters at 65.49934°N, 16.70224°W, formed after glaciation had retreated from the main (subglacially erupted) ediface of Heilagsdalsfjall (Sæmundsson et al., 2012).

Olivine and clinopyroxene crystals containing melt inclusions were ex-

tracted from each sample. The total carbon content of a melt inclusion is partitioned between the glass and vapour bubble (if present). Following Hartley et al. (2014), crystals were sequentially prepared for micro-Raman analysis of CO_2 vapour density in the bubbles, Secondary Ion Mass Spectrometry (SIMS) to determine carbon and trace element concentrations in the glass, and electron probe microanalysis (EPMA) to determine the major element chemistry of the inclusions and their crystal hosts. In the absence of an instrument-specific calibration for the Raman analyses, we do not quantify the mass of CO_2 hosted in the bubbles. However, where CO_2 vapour is detected in a bubble, the carbon concentration in the melt inclusion glass represents only a minimum estimate of the magmatic carbon budget at the time of inclusion entrapment. Full information on sample preparation and analytical setup is given in Supplementary Text A. In Supplementary Text B we explain why we do not apply a correction based on predicting the CO_2 vapour density in bubbles. Since we are primarily interested in trace element ratios, and carbon concentrations at the time of eruption, we do not apply post-entrapment crystallisation corrections (though we provide sufficient information in Supplementary Table 1 that the calculations may be performed).

3. Results

Melt inclusion C and Ba concentrations are shown for each eruption in Figure 2. All four eruptions show considerable variation in their C/Ba ratios, but only Háleyjabunga and Stapafell display positive correlations between C and Ba. Only three Háleyjabunga melt inclusions analysed by SIMS con-

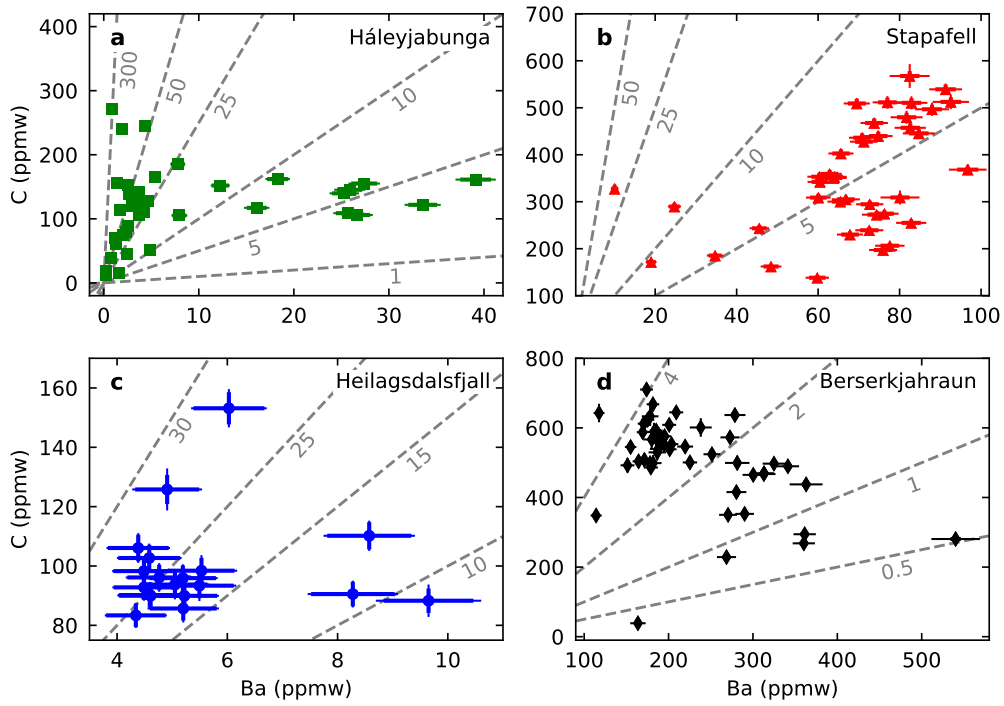

Figure 2: Melt inclusion glass C concentrations plotted against Ba concentration for each of the four eruptions studied here. The dashed grey lines indicate constant C/Ba ratio. Error bars show 1 s.d. combined precision and accuracy (thin lines) and 1 s.d. precision (bold lines).

tained bubbles in which CO_2 vapour was detected, a further three were measured by Raman only. Though five Stapafell melt-inclusion-hosted bubbles contained CO_2 vapour, only one was in an inclusion analysed by SIMS. No CO_2 vapour was detected in any of the bubbles hosted in Heilagsdalsfjall inclusions. Many of the Berserkjahraun inclusions contained bubbles in which CO_2 vapour was detected.

Trace element concentrations in the four melt inclusion suites are shown in Figure 3. Melt inclusions from Háleyjabunga (Figure 3a) show extreme vari-

ability in relative trace element enrichment, Maclennan (2008b) and Neave et al. (2018) demonstrated the variability is most likely mantle-derived. Four Háleyjabunga inclusions have anomalously high Ba and Nb concentrations relative to the light rare-earth elements; since their carbon concentrations are similar to the main population of inclusions they have not retained high C/Ba or C/Nb ratios. The Háleyjabunga inclusion with the highest C/Ba ratio is part of a sub-population of three inclusions with higher carbon concentrations. Ignoring this anomalous inclusion, the highest C/Ba ratios (>55) are observed in inclusions with depleted trace element patterns, though they are not anomalously depleted among the larger population of Háleyjabunga inclusions.

The Stapafell inclusions with highest C/Ba (Figure 3b) show trace element patterns with anomalously low Ba and Nb concentrations relative to the light and middle rare earth elements. Despite the anomalous trace element patterns of this small number of inclusions, Ba, Nb and C appear not to be fractionated from each other, discussed further in Section 6.1. The Stapafell melt inclusions show enriched trace element patterns, and our new observations are consistent with the conclusions of Neave et al. (2018) that the variability is not mantle derived, but largely reflects variable crystal fractionation.

The Heilagsdalsfjall melt inclusions (Figure 3c) show little trace element variability, and are strongly depleted in incompatible trace elements. Berserkjahraun melt inclusions (Figure 3d) show the most extreme enrichments in incompatible trace elements of the four eruptions, and show little mantle-derived variability among the inclusions. The small Sr- and Zr-

anomalies seen in many of the inclusions from all four eruptions are likely the result of interaction with plagioclase in the crust (Aigner-Torres et al., 2007).

4. Eruption specific processes controlling C-Ba systematics

Before considering the trends defining the local (Icelandic) and global C/Ba and C/Nb arrays, we consider individually the carbon-trace element systematics of each of our new datasets from Háleyjabunga, Stapafell, Heilagsdalsfjall, and Berserkjahraun.

The melt inclusions from Háleyjabunga display C-Ba systematics that are consistent with partial degassing and mixing, as proposed by Matthews et al. (2017). A positive correlation between the melt inclusion Ba and C concentrations exists, and is strongest in the most Ba-depleted inclusions, with an average gradient of ∼35-40 (Figure 2a). Furthermore, the Ba concentration in the inclusions has increasing variance as their C content increases. Three Háleyjabunga melt inclusions form a sub-population with higher carbon concentrations than the other Háleyjabunga melt inclusions. The higher carbon contents seen in this sub-population may reflect inclusion entrapment at an earlier stage of magma evolution; magmas may lose carbon as they evolve, either due to degassing driven by their ascent towards the surface, or by progressive mixing with low-carbon melts.

Where a melt inclusion population has been subject to partial degassing and mixing, Matthews et al. (2017) argued that the highest C/Ba ratio seen in the dataset is the most likely to preserve the mantle value. However, the highest C/Ba values seen within the Háleyjabunga inclusions have the

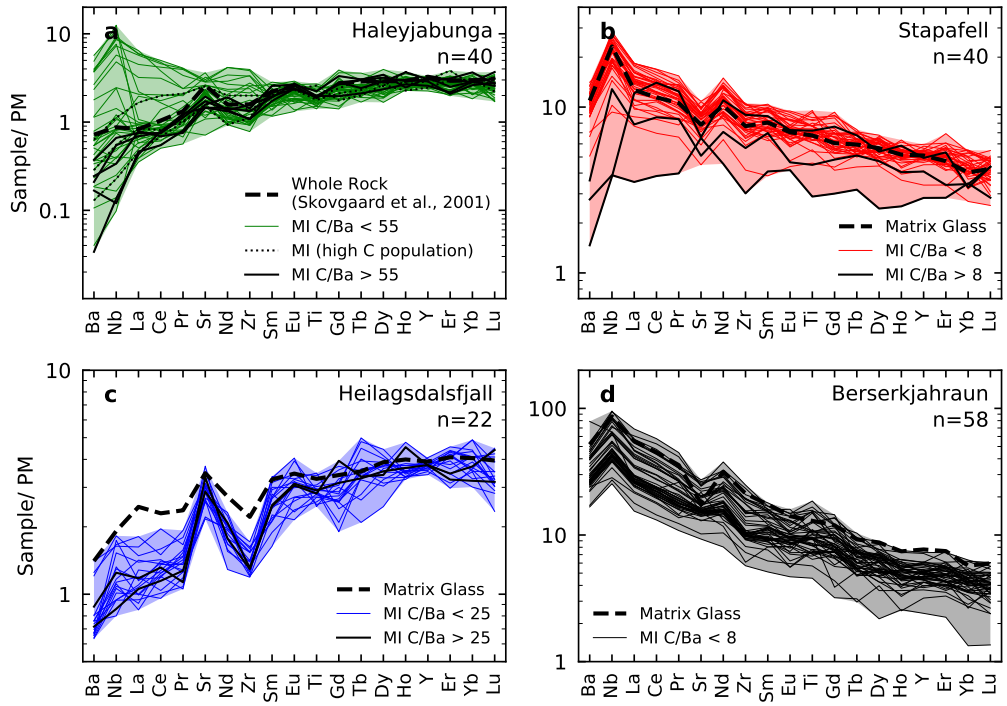

Figure 3: Normalised melt inclusion trace element concentrations. The region between the most extreme melt inclusions of each eruption is shown by shading. Also shown (as thick dashed lines) are the means of matrix glasses analyses for Stapafell, Heilagsdalsfjall and Berserkjahraun, and the whole rock analysis of Háleyjabunga reported by Skovgaard et al. (2001). The melt inclusions preserving the highest CO_2/Ba ratios are highlighted in black, with the threshold CO_2/Ba used reported in the legend for each panel. All analyses are normalised to the primitive mantle of Palme and O'Neill (2003).

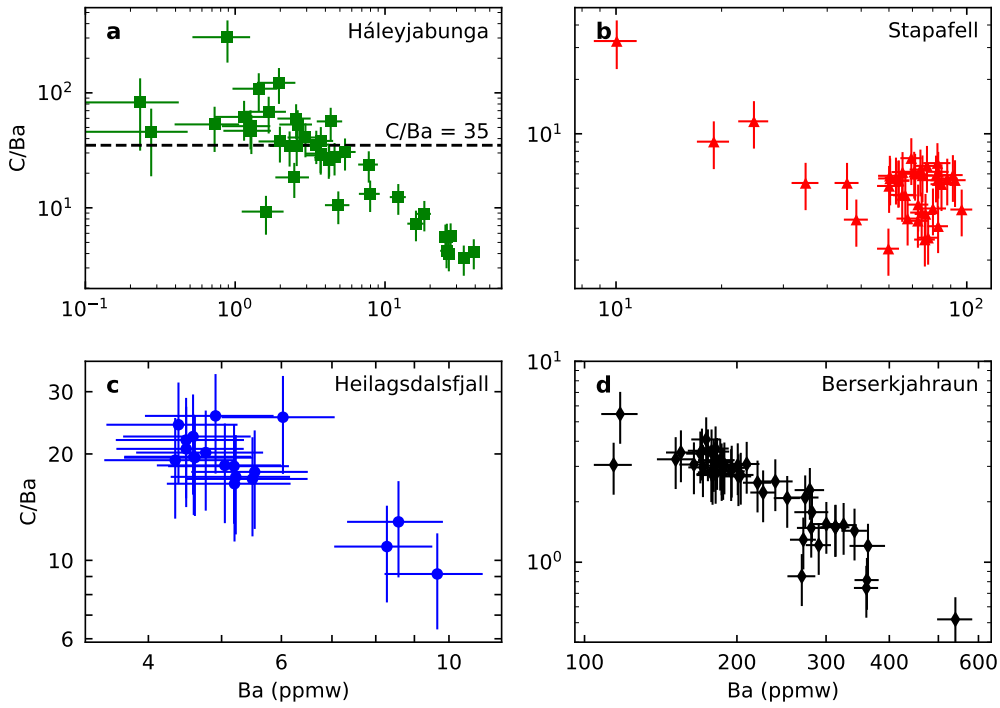

Figure 4: Melt inclusion glass C/Ba ratios for each of the four eruptions studied here. The error bars show the 2 s.d. combined accuracy and precision; the correlated nature of the uncertainties is not shown here, but is shown in Figure 5.

greatest uncertainty (Figure 4). The strong C-Ba correlation seen in the most depleted Háleyjabunga inclusions defines a C/Ba ratio of ∼35 (Figure 2a), and many of the inclusions that record higher C/Ba ratios are within 2 s.d. uncertainty of 35 (Figure 4). Despite the consistency in C/Ba among most of the inclusions, the three inclusions with highest C/Ba ratios (100-300) are not within uncertainty of 35, demonstrating that Háleyjaunga has retained C/Ba heterogeneity extending to both high and low values of the ratio.

Like the inclusions from Háleyjabunga, a subset of the Stapafell inclusions

show a strong positive correlation between C and Ba (Figure 2b), defined by a C/Ba ratio of ∼6 (Figure 4b). In contrast to Háleyjabunga, the Stapafell inclusions do not show the increasing variance in Ba concentration with increasing C content, probably due to the Stapafell melt inclusions recording a more prolonged history of mixing and fractional crystallisation. Whilst most of the Stapafell inclusions have C/Ba ratios within uncertainty of 2.5-6.0, three bubble-uncorrected inclusions and one bubble-corrected inclusion have higher C/Ba ratios. However, these high C/Ba inclusions have anomalously low Ba and Nb concentrations (Figure 3b), and so should be viewed with caution.

The melt inclusions from Heilagsdalsfjall show very little variability in their trace element concentrations (Figure 3c), their carbon concentrations (Figure 2c), and consequently their C/Ba ratios (Figure 4c). This chemical homogeneity is most likely a product of efficient magma mixing during transport and storage. The carbon contents of the melt inclusions might reflect the pressure at which the magma was stored when the inclusions were trapped, if the magma was CO_2 vapour saturated. Alternatively, the carbon content may reflect mixing of CO_2 vapour-undersaturated melts with CO_2 vapour-saturated melts, as proposed by Matthews et al. (2017).

The Berserkjahraun inclusions preserve substantial variability in Ba concentration, but little variability in carbon concentration by comparison (Figure 2d). The carbon concentrations allow the majority of the melt inclusions to be divided into two groups, a more Ba-depleted higher-carbon group (150-250 ppmw Ba; ∼600 ppmw C), and a more Ba-enriched lower-carbon group (250-400 ppmw Ba; ∼400 ppmw C). These two groups of inclusions

also cluster into distinct C/Ba groups (Figure 4d). This pattern of carbon and trace element concentrations is consistent with the inclusions recording variably evolved magmas, perhaps at two different storage depths. Whilst CO_2 vapour saturation pressures can be calculated for each group of inclusions, they are unlikely to correspond to the pressures of magma storage; the prevalance of CO_2 vapour within bubbles in the inclusions indicates the magmas were much more carbon rich, and likely to have undergone (perhaps multiple) episodes of decrepitation during ascent.

5. Systematics of the Global Melt Inclusion Array

In Figure 5 we compare our new dataset of C/Ba ratios from the Háleyjabunga, Stapafell, Heilagsdalsfjall, and Berserkjahraun melt inclusions, with other Icelandic melt inclusion suites and those from ocean-island and mid-ocean ridge settings. We exclude inclusions from arc volcanoes since their enrichment in H_2O complicates our understanding of CO_2 solubility.

In both the Icelandic compilation (Figure 5a) and the global compilation (Figure 5b), there is a striking negative correlation between C/Ba and Ba concentration. The array is bounded above and below by lines of constant carbon concentration, though bubble-corrected inclusions (unfilled symbols) break through this upper bound. For the most depleted inclusions the low bound corresponds to approximately 30 ppmw carbon, and the high bound to 300-400 ppmw carbon. The same systematic is observed in C/Nb-Nb space (Supplementary Figure 1).

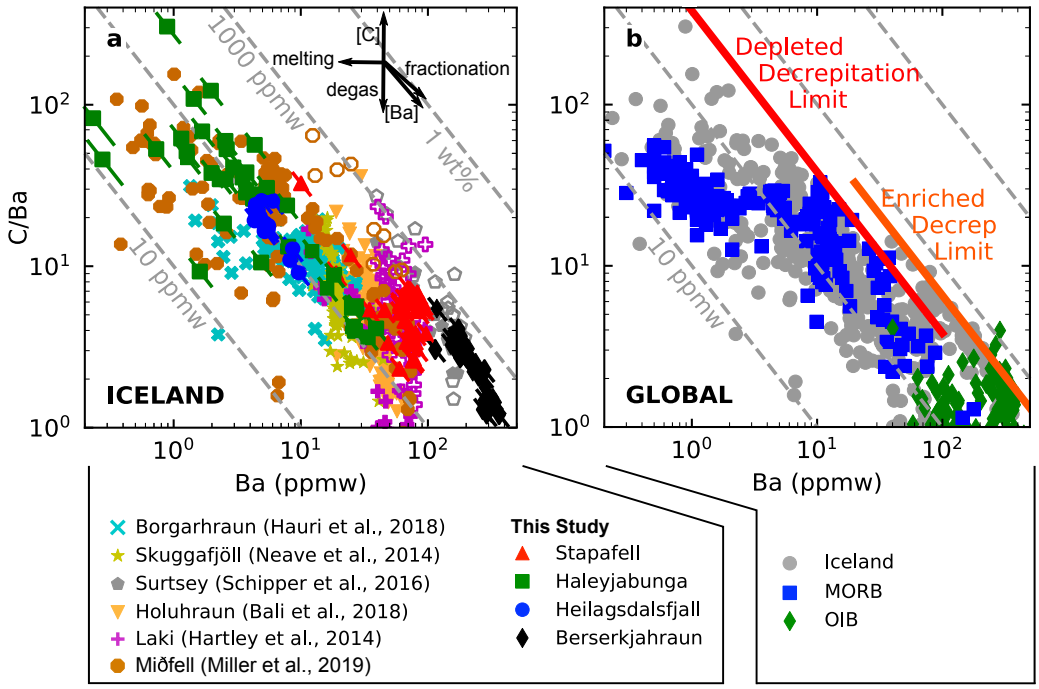

Figure 5: C/Ba ratios in the melt inclusion glass for the four eruptions studied here, and compiled data from other eruptions in Iceland (panels a and b), from along the mid-ocean ridge system (MORB), and from ocean-islands (OIB) (panel b). Filled symbols show values for C/Ba derived from carbon hosted in the glass only, open symbols show the values of C/Ba where bubbles (measured by Raman) have been added back to the glass. The vectors in panel a show the effects of mantle melting, fractionation during melting, CO_2 degassing, C addition, and Ba addition. Diagonal dashed-grey lines show constant carbon concentration (10 ppmw, 100 ppmw, 1000 ppmw and 1 wt%). Error bars on the data from this study show the correlated 1 s.d. uncertainty (combined accuracy and precision) between Ba and C/Ba. Solid red and orange lines in panel b show the inferred decrepitation limits at 380 ppmw and 660 ppmw C, respectively. Most OIB data falls off the bottom of the figure due to low C concentrations. Data from Hauri et al. (2018); Hartley et al. (2014); Neave et al. (2014); Schipper et al. (2016); Bali et al. (2018); Le Voyer et al. (2017); Saal et al. (2002); Sides et al. (2014); Wanless and Shaw (2012); Wanless et al. (2014); Cabral et al. (2014); Métrich et al. (2014); Wanless et al. (2015); Tucker et al. (2019).

5.1. A spurious correlation?

In Figure 5 we compare melt inclusion C/Ba ratios with their Ba concentrations. The potential for spurious correlations resulting from the presence of the same variabile on both y and x axes is well known (e.g., Jackson and Somers, 1991). In this study we are interested in the controls on the quantity C/Ba, as it has been used extensively in the estimation of mantle carbon concentrations. Whilst we could use indices of eruption enrichment that do not involve the Ba concentration, e.g., La/Sm, or Ce/Y, they both nonetheless scale with Ba concentration and so are not truly independent. By using Ba concentration as our index for eruption enrichment we can still identify 'spurious' correlations by plotting lines of C concentration directly on Figure 5; indeed, the fact that the data parallel the constant C concentration lines in on Figure 5 demonstrates that the global array is being controlled by variable Ba concentration at roughly constant C concentration, an important observation.

5.2. A global array reflecting mantle carbon heterogeneity?

The negative correlation between C/Ba and Ba concentration could be caused by source heterogeneity: the array being generated by mixing between a trace-element-depleted high-C/Ba endmember and a trace-element-enriched low-C/Ba endmember. In this scenario, the trace-element enriched mantle reservoirs that contribute disproportionately to the Ba-enriched melts would not have corresponding C-enrichments.

However, the negative C/Ba-Ba correlation has the same position and gradient in both the Icelandic and global datasets. If the array was generated solely by mantle C/Ba heterogeneity, the coincidence of local and

global C/Ba (and C/Nb) arrays would imply two things. First, depleted and enriched mantle components occur with the same distinct C/Ba and C/Nb ratios everywhere. Second, the melting process must consistently produce enriched endmember melts with similar Ba and Nb concentrations, and depleted endmember melts with similar Ba and Nb concentrations, to produce mixing arrays with the same slope in different locations. Radiogenic isotope constraints demonstrate that there is substantial variation in the chemistry of enriched and depleted components globally, even between highly-incompatible elements that are difficult to fractionate during partial melting (e.g., U and Rb; Stracke et al., 2005). It seems unlikely, therefore, that these diverse mantle components would be characterised by single values of the C/Ba and C/Nb ratios.

Alternatively, the melting process and source C/Ba and C/Nb must covary between locations, such that they always produce endmember melts falling along the global array. Given the complexities of mantle melting, melt transport, and melt mixing processes (e.g., Maclennan et al., 2003b; Wanless et al., 2014; Shorttle, 2015), and the apparent independence of mantle composition and aggregate melt fraction in global datasets (e.g., Gale et al., 2014), this scenario seems very unlikely.

5.3. A global array controlled by the melting process?

Could the melting process be responsible for generating the global array, in absence of coupled variation in source composition and melting process? If mantle melting can consistently produce melts with carbon concentrations no higher than ∼700 ppmw over the large range of Ba concentrations preserved by melt inclusions, it could reproduce the global C/Ba array. Such a scenario

might occur during graphite-saturated melting (e.g., Eguchi and Dasgupta, 2018b). However, the Fe^{3+}/Fe^{2+} ratios of basalts and melt inclusions from MORB and ocean islands indicate the mantle is not sufficiently reduced for graphite-present melting to occur ubiquitously (Bézos and Humler, 2005; Cottrell and Kelley, 2011; Shorttle et al., 2015; Berry et al., 2018; Moussallam et al., 2019).

Furthermore, the presence of CO_2-rich shrinkage bubbles in a large proportion of the melt inclusions demonstrates that many of the melts must have had more carbon in the past, which would have placed them above the global array. Bubble-corrections applied to the inclusions from Berserkjahraun, Miðfell, Laki and Surtsey, demonstrate how significant this effect can be (Figure 5a). The global array cannot, therefore, be generated by the melting process alone, though there may be a role for graphite-present melting in the generation of anomalously high C/Ba and C/Nb ratios (Section 6.2).

5.4. A global array controlled by degassing?

A simpler explanation than source heterogeneity (or graphite-present melting) calls for a process that limits the carbon concentration within the melt inclusion. The most obvious process is CO_2 vapour degassing. In this case, the lower limit of carbon on the array corresponds to CO_2 solubility for magma storage in shallow crustal magma chambers pre-entrapment. The small number of inclusions with lower carbon concentrations than this probably owe their undersaturation to degassing during eruption, or mixing with extremely carbon-depleted partial mantle melts (Matthews et al., 2017).

The upper bound on the carbon concentration in trace-element depleted

melt inclusions (300 ppmw C) corresponds to CO_2 vapour-saturation pressures in the range of 1-3 kbar, depending on the solubility model chosen (Figure 6, Supplementary Figure 2). This pressure range coincides with that expected for olivine decrepitation (Wanamaker et al., 1990; Maclennan, 2017), where the crystal undergoes brittle failure when it can no longer support the pressure difference between the inclusion and its surroundings. Experiments performed by Wanamaker et al. (1990) show that olivine may support overpressures of up to 2.2 kbar. This is close to the maximum entrapment pressure of the moderately-depleted inclusions when calculated with the CO_2 solubility model of Iacono-Marziano et al. (2012), shown in Figure 6.

Figure 5b demonstrates the presence of two different upper limits; one for melt inclusions from the more trace-element depleted eruptions and one for melt inclusions from the more enriched eruptions. If decrepitation is responsible for the upper limit of the array, the limits for both enriched and depleted eruptions ought to correspond to the CO_2 solubility at the decrepitation limit ($\sim$2.2 kbar). However, the dependence of CO_2 solubility on melt composition allows significantly different carbon concentrations to equilibrate at the same CO_2 partial pressure in different melts. Melt polymerisation tends to reduce CO_2 solubility, whilst the presence of cations with an affinity for forming carbonate complexes increases CO_2 solubility (Shishkina et al., 2014).

The trace-element enriched inclusions are significantly richer in total-alkalis (Na_2O + K_2O) for similar SiO_2 contents (Supplementary Figure 3), but this does not translate into significant differences in the π^* compositional parameter used by Shishkina et al. (2014) in their CO_2 solubility model (Supplementary Figure 4). Though the concentration of alkali elements in the

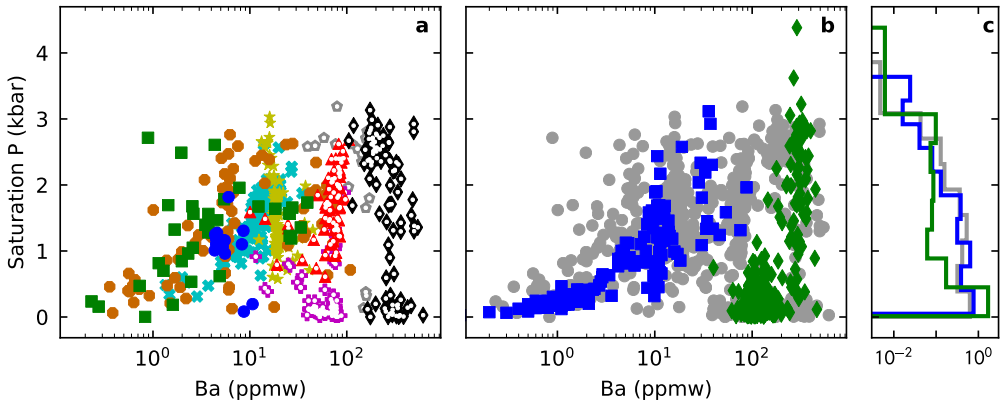

Figure 6: The pressure of CO_2 vapour saturation for each melt inclusion in the Iceland compilation (panel a), and the global compilation (panels b and c). Symbols as used in Figure 5. Saturation pressures for melt inclusions from depleted Icelandic eruptions and MORB are calculated using the CO_2 solubility model by Iacono-Marziano et al. (2012). Saturation pressures for melt inclusions from enriched Icelandic eruptions (symbols overlaid by white dots in panel a) and OIB are calculated using the power-law fit to experimental data for 'Sunset Crater' by Allison et al. (2019). The effect of H_2O is neglected in all calculations, as the melts contain sufficiently low H_2O concentrations that CO_2 solubility will be little affected. The calculations do not include bubble-corrections.

enriched inclusions acts to increase CO_2 vapour solubility, their lower MgO and CaO concentrations tends to decrease CO_2 vapour solubility (Dixon, 1997). As the decrepitation limit should not vary strongly with eruption enrichment, it is likely that the higher bounding carbon concentration for the enriched melts is solubility related, even if not captured by π^*.

A compositional-solubility effect creating the different bounds to the global array is supported by recent experimental work by Allison et al. (2019). By performing new experiments at intermediate pressure and alkaline compositions, Allison et al. (2019) showed that the existing CO_2 solubility models provide inadequate predictions of CO_2 solubility in more alkaline melts. Though the least alkaline experimental melt composition used by Allison et al. (2019) is more alkaline than the majority of melt inclusions displayed in Figure 5, their empirical expression for CO_2 solubility likely incorporates other compositional effects of importance for the more enriched eruptions considered here. Figure 6 demonstrates that applying the empirical expression to the more enriched eruptions brings their saturation pressures into line with the depleted eruptions, when the CO_2 solubility model by Iacono-Marziano et al. (2012) is applied to the inclusions from depleted eruptions. However, a discrepancy exists if the saturation pressures for depleted eruptions are calculated using the models by Shishkina et al. (2014) or Eguchi and Dasgupta (2018a) (Supplementary Figure 2).

Whilst we think olivine-decrepitation offers the most likely explanation for the structure of the Icelandic and global C/Ba arrays, our argument would be stronger if a single solubility model were able to account for the offset in maximum carbon content of the depleted and enriched eruptions. Though

we have shown that simultaneous application of the Iacono-Marziano et al. (2012) solubility model for the depleted eruptions, and the Allison et al. (2019) solubility model for the enriched eruptions, brings the upper-limit of the calculated saturation pressures for the depleted and enriched eruptions into line, this upper-limit is significantly higher than the experimental decrepitation threshold ($\sim$2.2 kbar, Figure 6). Despite the Allison et al. (2019) model being calibrated on more alkaline magmas than found in our enriched inclusions, the success of our calculations demonstrates the plausibility that the existing solubility models do not fully capture the compositional dependence of magmatic carbon solubility. As neither heterogeneity in mantle carbon, nor melting processes, are able to satisfactorily explain the observations, leaving olivine-decrepitation as the most viable mechanism for generating the global C/Ba array.

6. The origin of high C/Ba and C/Nb ratios

The gross structure of both the Icelandic and global melt inclusion arrays shown in Figure 5 is primarily controlled by low-pressure processes: storage in shallow magma chambers and olivine decrepitation (Section 5). However, many eruptions sit almost entirely within the bounds imposed by shallow storage and decrepitation, or have partitioned a significant fraction of their CO_2 budget into bubbles, thereby overcoming the decrepitation threshold. Many of these datasets may still preserve the C/Ba ratios of their melts at the time of entrapment. The two most depleted eruptions in the Icelandic compilation (Miðfell and Háleyjabunga) have C/Ba ratios exceeding 100, extending to much higher values than seen in other MORB and OIB melt

inclusions. In this section we consider the likelihood of such high C/Ba ratios reflecting mantle C/Ba, as Miller et al. (2019) previously suggested to be the case for the Miðfell melt inclusions.

6.1. Can fractionation during mantle melting generate high C/Ba and C/Nb ratios?

Whilst C, Ba, and Nb are all thought to be highly incompatible during mantle melting, experimental work by Rosenthal et al. (2015) suggests that during mantle melting carbon should behave marginally more compatibly than Ba, and less compatibly than Nb. Melts produced by very small degrees of melting may, therefore, obtain extreme C/Ba or C/Nb ratios by fractionation. If it can be demonstrated that Nb and Ba have not been fractionated from each other during melting, then it is also unlikely that carbon was fractionated from either (Miller et al., 2019). Fractionation of Ba and Nb will generate co-variations of the Ba/Nb ratio in the magmas with their Ba and Nb concentration. Figure 7a shows this is not seen in any of the eruptions in this study, or the other Icelandic eruptions in the compilation. The scatter in Ba/Nb ratio arises largely from analytical imprecision, but could also reflect small scale source heterogeneity. The role of analytical precision in generating the extreme C/Ba and C/Nb ratios is considered in Section 6.4.

Another approach to assessing elemental fractionation during melting is to compare the variability of trace element concentrations. The more incompatibly an element behaves during melting, the greater its variability amongst instantaneous fractional melts of the mantle. If two elements in a dataset have the same mean-normalised variance, the melting process has

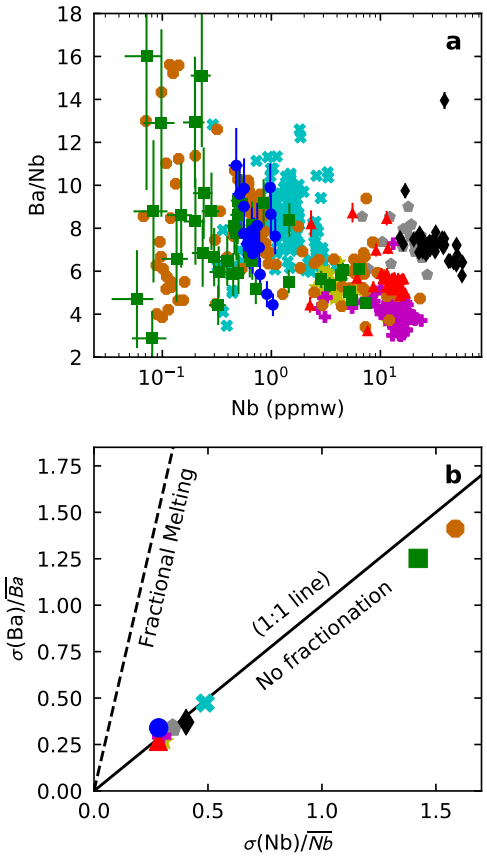

Figure 7: Panel a shows the Ba/Nb ratio of the melt inclusions from the eruptions in Figure 1. Three representative error bars are shown, illustrating the 1 s.d. precision on the Ba/Nb ratio and Nb concentrations with varying enrichment, calculated from variably enriched secondary standard analyses. The highest Ba/Nb values for Miðfell (Miller et al., 2019) fall off the top of the plot. Panel b compares the standard deviation of Ba and Nb in melt inclusions from each eruption, normalised to their mean. The solid line shows the expected relationship if the two elements are not fractionated from each other during melting, the dashed line shows the expected relationship if they are fractionated by perfect fractional melting (Rudge et al., 2013), using the partition coefficients from Workman and Hart (2005).

not fractionated the elements from each other (Rudge et al., 2013). The relative variance of Ba and Nb for each Icelandic melt inclusion suite are shown together in Figure 7b, providing further evidence that Ba and Nb have not been fractionated from each other. Elements more compatible than Nb have been fractionated from each other, as demonstrated by their relative variances (Supplementary Figure 5). Whilst this analysis is strictly valid only for melts from a homogeneous mantle, it nonetheless demonstrates that the primary signal in the trace-element variance structure is from the melting process (Supplementary Text C).

Assuming that the behaviour of carbon during mantle melting can be modelled as an incompatible element, and that it has a partition coefficient between that of Ba and Nb (Rosenthal et al., 2015), the apparent lack of fractionation between Ba and Nb would suggest that primary magmatic C/Ba and C/Nb ratios will record mantle source ratios. Additionally, Miller et al. (2019) argued that if carbon were fractionated from Ba and Nb, then high values of C/Ba should not be associated with high values of C/Nb. If carbon were, instead, to behave more compatibly than both Ba and Nb, the most depleted melts could acquire C/Ba and C/Nb ratios higher than their source. We consider this possibility below.

6.2. Are high C/Ba and C/Nb ratios the product of graphite-saturated melting?

One scenario in which carbon would behave considerably more compatibly than both Ba and Nb during melting is if conditions were sufficiently reducing for graphite or diamond to be stabilised. The stability of carbonate over graphite is controlled by the oxygen fugacity (fO_2) of the mantle

(e.g., Dasgupta and Hirschmann, 2010). Eguchi and Dasgupta (2018b) modelled the chemical effects of melts from a graphite-saturated mantle source contributing to basalts, concluding that such models provide a poor fit to natural MORB and OIB. They therefore inferred that graphite-saturated melts do not generally contribute to basaltic volcanism. By incorporating graphite saturation into the model used by Matthews et al. (2017) we extend the work of Eguchi and Dasgupta (2018b) by assessing how the signal of graphite-saturated melts might be modulated by the mixing and degassing processes, and subsequently manifested in a suite of melt inclusions.

A full description of the general properties of the concurrent degassing and mixing calculations is provided in by Matthews et al. (2017), and a description of how the model is extended for graphite-saturated melting is provided in Appendix A. First, we use a melting model (Katz et al., 2003) to generate the masses and compositions of instantaneous melts produced from a column of upwelling mantle, assuming that melting is near-fractional, and that the mantle has 30 ppmw carbon. Examples of the melting model output, for variable fO_2, are shown in Figure 8. The presence of graphite during melting decreases the carbon content of the most enriched melts, and increases the carbon concentration in the more depleted melts, up until graphite is exhausted.

The second stage of the model emulates the transport of the instantaneous melts into a crustal magma reservoir. Any melts with a carbon concentration in excess of the carbon content at CO_2 vapour saturation have carbon removed until they return to saturation. The melts are then allowed to partially mix, modelled using the properties of the Dirichlet distribution (Rudge

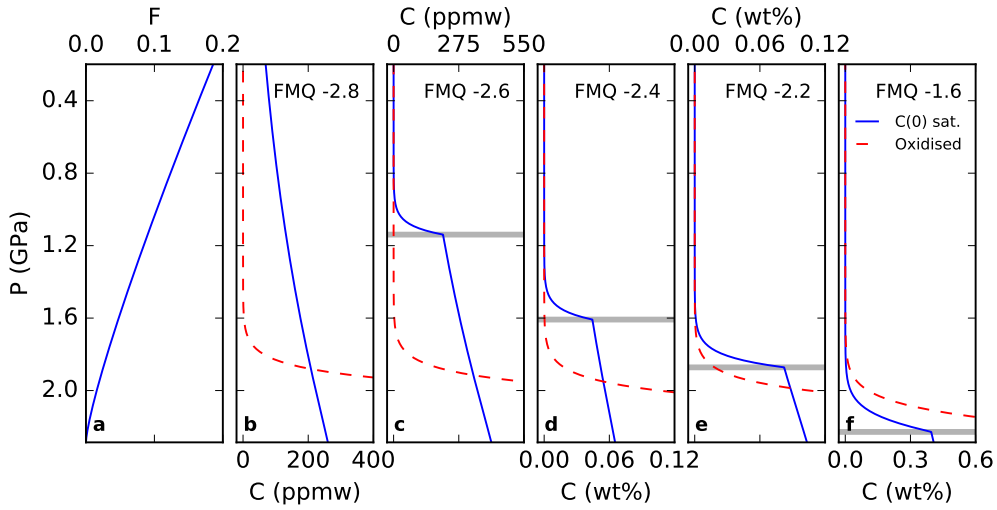

Figure 8: Panel a shows the melt fraction as a function of pressure, calculated as described in the main text. The solid blue lines in panels b-f show the calculated carbon concentration of melts generated at variable oxygen fugacity, buffered relative to the FMQ buffer. The mantle carbon content is set to 30 ppmw. Below the grey line the mantle is graphite saturated. The red dashed line shows the concentration of carbon in the melts in a mantle sufficiently oxidised that graphite is never saturated during melting, i.e. the result used in the main text of this paper. Note that different scales are used on the x-axis in each panel.

et al., 2013). Since the degassing step substantially reduces the carbon concentration of the most enriched melts in most runs of the model, the most pronounced effect of graphite saturation is on the depleted melts. Depleted melts generated from a very reduced melting region have extremely high C/Ba ratios, far in excess of their mantle source (Figure 9).

The distributions of mixed melts shown in Figure 9 are, in some ways, similar to the distributions of real data: they preserve substantial C/Ba heterogeneity, there is a defined upper bound to the array corresponding to a fixed carbon concentration, and there is a low-probability tail of very high C/Ba melts. However, the presence of graphite strongly decouples the C concentrations in the melts from their Ba and Nb concentrations, destroying any correlation between them (Supplementary Figure 6). The presence of graphite during melting can, therefore, be ruled out for the generation of the majority of melts preserved in melt inclusions from Háleyjabunga and Stapafell (this study), and Borgarhraun (Hauri et al., 2018).

However, if a small part of the melting region remains graphite-saturated, it may contribute a small mass of melts with C/Ba exceeding the mantle value. Whilst such a small mass of melt is unlikely to influence the C-Ba systematics expressed by the majority of partially-mixed melts, a small number of melts may still preserve the high C/Ba ratios. It is then plausible that the extremely high C/Ba and C/Nb ratios measured in a small number of the Miðfell and Háleyjabunga inclusions reflect contributions from a low-mass-fraction mantle component that remains graphite-saturated during melting. We discuss the likelihood of such a component existing below.

If the carbon content of the Icelandic mantle is similar to that of the

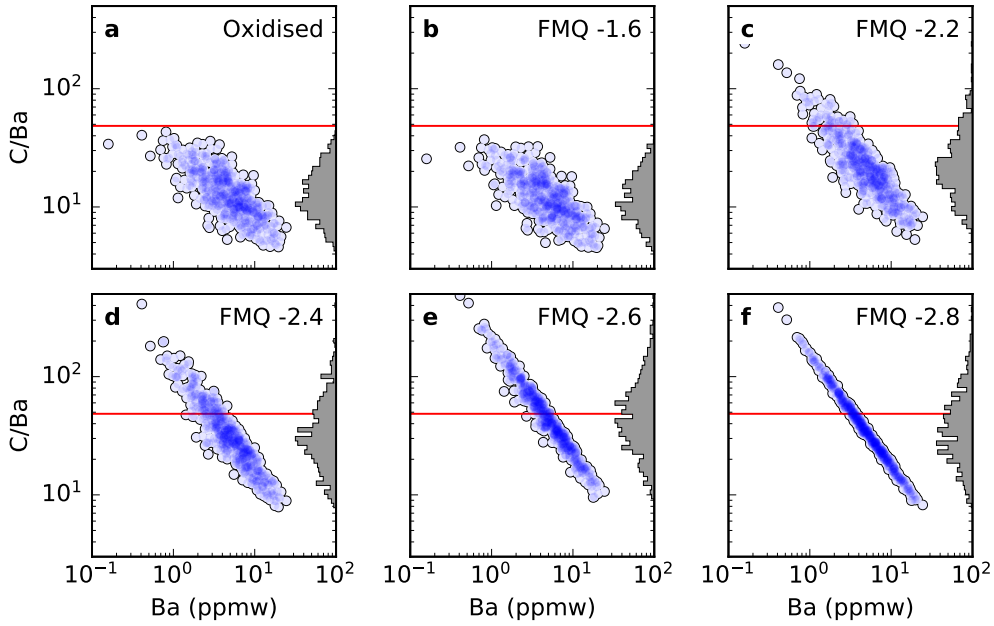

Figure 9: Results of the mixing and degassing model for instantaneous melts produced during graphite saturated melting of a single mantle source, followed by degassing at 2000 bar. The carbon content of the mantle is set at 30 ppmw. Panel a shows the results from melting without graphite present. Panels b-f show the results when melting in the presence of graphite (until it is exhausted from the residue) at variable oxygen fugacity, expressed in log-units relative to the quartz-fayalite-magnetite buffer. The horizontal red lines show the homogeneous source C/Ba ratio, which is constant for all scenarios at C/Ba = 48. The shading shows the density of samples drawn from the distribution.

depleted mantle (∼30 ppmw, e.g., Michael and Graham, 2015; Hauri et al., 2018; Hirschmann, 2018; Tucker et al., 2018), for graphite-saturated melting to occur the mantle must be significantly more reduced than indicated by $Fe^{3+}/\Sigma Fe$ ratios of Icelandic basalts (Shorttle et al., 2015), or MORB (Bézos and Humler, 2005; Cottrell and Kelley, 2011; Berry et al., 2018). However, if the mantle source of Háleyjabunga and Miðfell are much more carbon rich, as suggested by Miller et al. (2019), the high carbon budget may itself influence the redox equilibria (Cottrell and Kelley, 2013) via the reaction

$$C^0 + 2Fe_2O_3 \rightarrow CO_2 + 4FeO. \quad (1)$$

If the mantle source has been enriched in carbon due to the addition of reduced carbon, the oxidising capacity of the Fe^{3+} component of the mantle may be exhausted before all the reduced carbon has been converted to CO_2 or carbonate. Assuming there is 0.3 wt% Fe_2O_3 in the mantle (McCammon, 2005), 450 ppmw reduced carbon would be required to overwhelm the mantle's oxidising capacity, causing graphite to be sustained into the melting region. This value is within uncertainty of the carbon content inferred by Miller et al. (2019) for the 'deep' component contributing to Miðfell.

We emphasise that this high carbon content, and its implications for mantle redox, may apply only to a very small fraction of the Icelandic mantle, not ubiquitously sampled by Icelandic magmatism. Similarly, evidence for extremely reduced melts produced from a graphite-saturated mantle component would be rapidly erased by mixing with more oxidised (but carbon and trace-element depleted) melts of other mantle components. Cottrell and Kelley (2013) proposed a similar model to explain lower $Fe^{3+}/\Sigma Fe$ ratios in enriched MORB glasses; in their model reduced carbon was added to the

enriched mantle component contributing to the MORB melts, though their data did not require the mantle to be sufficiently reduced that melting would be graphite-saturated.

Whilst we cannot rule out that the high values of C/Ba and C/Nb are derived from graphite-saturated melting, this scenario necessitates anomalously reduced mantle for which there is no evidence, but could be a natural consequence of extreme reduced carbon enrichment. If graphite is present during the production of some of the magmas contributing to Háleyjabunga and Miðfell, the C/Ba observations would not quantitatively constrain the C/Ba of the mantle source. However, the high C/Ba ratios would nonetheless suggest some component of the Icelandic mantle has an unusually high (reduced) carbon budget compared with the MORB mantle.

6.3. Is melt 'regassing' by CO_2 vapour a viable mechanism for generating high C/Ba and C/Nb ratios?

In the models described by Matthews et al. (2017) and used in Section 6.2, a significant mass of CO_2 vapour is generated by degassing of the most carbon and trace-element enriched magmas. Whilst we have implicitly assumed this vapour immediately leaves the system, likely through fractures in the crust, it is conceivable that the vapour might, instead, be absorbed by co-existing CO_2 vapour-undersaturated depleted-melts. Such a 'self-regassing' process will tend to drive the C/Ba and C/Nb ratios of the most depleted melts to very high values, whilst having no effect on the more enriched CO_2-vapour saturated inclusions. The expected C-Ba systematics will, therefore, be qualitatively similar to those shown for graphite-saturated melting in Figure 9.

Whilst we cannot definitively discount regassing contributing to the generation of high C/Ba and C/Nb ratios, we can assess its likelihood. For exsolved vapour to successfully regas a CO_2 vapour-undersaturated depleted magma a number of conditions must be satisfied. First, the depleted magma must coexist spatially and temporally with the enriched magma from which the CO_2 vapour is derived. Given the evidence for concurrent mixing and crystallisation in Icelandic magmatic systems (Maclennan, 2008a) this seems likely to be true once the magmas have stalled in a magma reservoir. However, CO_2 vapour may be continually lost from the enriched melts during transport. Since the enriched melts may be transported separately from the depleted melts, CO_2 vapour loss from the enriched melts may occur prior to their juxtaposition with depleted melts. Second, the depleted magmas must lie spatially above the enriched magmas, as the exsolved CO_2 vapour will be buoyant. Mixing of magmas likely involves considerable convective stirring, and so this seems likely for at least some of the melts at any instant in time. Finally, the timescale of bubble ascent and escape must be long relative to the timescale for bubble resorption. How likely this final condition is to be satisfied is much more uncertain.

If self-regassing was responsible for the high C/Ba and C/Nb ratios in Háleyjabunga and Miðfell, we might expect to see evidence for its occurrence in other eruptions. Melt inclusions from Borgarhraun (northern Iceland) have also retained substantial mantle-derived trace-element variability (Maclennan et al., 2003a), which was gradually homogenised throughout crystallisation (Maclennan, 2008a), indicating the juxtaposition of depleted and enriched melts prior to eruption. However, no evidence for self-regassing is seen

in the melt inclusion carbon-trace element systematics (Hauri et al., 2018). We conclude, therefore, that whilst impossible to rule out, self-regassing is an unlikely explanation for high C/Ba and C/Nb ratios.

6.4. Are high C/Ba and C/Nb ratios analytical artefacts?

The highest C/Ba and C/Nb ratios are seen in the most trace-element depleted inclusions. Where concentrations of trace elements are low, fewer counts are recorded during analysis, propagating to much poorer precision in C/Ba and C/Nb ratios, as demonstrated by the error bars in Figures 4 and 5, and Supplementary Figure 1. Whilst the precision is poorer for both C/Ba and C/Nb in the most depleted inclusions, the lower count rates for Nb relative to Ba results in C/Nb having poorer precision than C/Ba (Supplementary Text A).

Error bars representing the 1 s.d. precision for C/Ba are shown for the four eruptions from this study in Figure 5. The magnitude of the uncertainties are likely to be similar for the compilation of carbon and trace-element data from Icelandic eruptions, having been measured using similar protocols. Even when the higher uncertainty in the C/Ba of the most depleted inclusions is considered, inclusions from Háleyjabunga and Miðfell show a robust offset to higher C/Ba relative to the other Icelandic melt inclusion suites. Whilst it is possible that we underestimate the uncertainty on the analysis, the precision calculated from counting statistics compares well with the empirical reproducibility of the secondary standard C/Ba (Supplementary Text A).

The analyses of carbon concentrations might also be susceptible to analytical artefacts. Unlike the Ba and Nb analyses, the carbon analyses for

the high C/Ba and C/Nb inclusions have the best counting statistics of the dataset, negating analytical precision as an issue. Rosenthal et al. (2015) suggested that the analyses resulting in the highest values of carbon concentration may have incorporated carbon derived from cracks in the sample. Avoiding making analyses in the vicinity of cracks (identified optically and in back-scatter electron images), as done in this study, minimises the likelihood of additional counts arising in this manner. Furthermore, the ^{12}C count rates are likely to vary erratically from cycle to cycle in such a situation, allowing the effect of contamination to be identified. No irregularity in the ^{12}C count rate was observed in the suite of melt inclusions presented here. Additionally, our carbon analyses define clearly an upper limit of 660 ppmw, carbon contamination would erase such a clear bound on the dataset, further suggesting the analyses are robust.

We therefore suggest it is more likely that the highest C/Ba ratios instead reflect sampling of low probability-density tail to the C/Ba distribution, i.e., those melts retaining a C/Ba ratio close to the source value (Matthews et al., 2017). However, we acknowledge that the high tail of the distribution may reflect graphite-saturated melting (Section 6.2) or CO_2 vapour regassing (Section 6.3).

6.5. Implications of a high C/Ba and C/Nb mantle component

In the previous sections we have described how the gross structure of the global melt inclusion C/Ba and C/Nb arrays is controlled principally by crustal processes, i.e., shallow-degassing and melt inclusion decrepitation. We have also shown that even within the confines of this array the maximum C/Ba ratios recorded by eruptions varies substantially, with two eruptions

from Iceland (Háleyjabunga and Miðfell) preserving C/Ba and C/Nb ratios considerably higher than seen elsewhere in Iceland (including the similarly depleted Borgarhraun eruption, Hauri et al., 2018), among ocean islands, or elsewhere on the mid-ocean ridge system. Decrepitation does not control the maximum C/Ba and C/Nb values of the most depleted eruptions; the maximum C/Ba and C/Nb values fall far below the decrepitation threshold (Figure 5). However, there is no unique interpretation for what this means for mantle carbon budgets. Here we set out some of the possible interpretations, but leave a full quantitative treatment for future work.

6.5.1. Ubiquitously high mantle C/Ba

Matthews et al. (2017) proposed that concurrent mixing and degassing may be operating ubiquitously on both melt inclusion and submarine glass suites. Whilst it is possible to identify concurrent mixing and degassing in some datasets, it is generally challenging to rule it out conclusively. Following this logic, we might suggest that the extreme depletion in trace elements of the melt inclusions from Háleyjabunga and Miðfell have enabled these eruptions to preserve typical mantle C/Ba and C/Nb values. This is similar to an argument made by Matthews et al. (2017); they suggested a single mantle C/Ba of ∼40 was consistent with all the available melt inclusion and submarine glass suites available at that time. The high C/Ba ratios observed in Háleyjabunga and Miðfell inclusions demonstrates that a single C/Ba ratio of ∼40 is not representative of the whole mantle. However, a C/Ba ratio of ∼140 would be consistent not only with the inclusions from Háleyjabunga and Miðfell (Figure 4), but also with all the other melt inclusion suites (Figure 5), their lower C/Ba ratios then being a product of degassing and mixing.

The evidence upon which Matthews et al. (2017) based their conclusion was the coincidence of the maximum C/Ba ratio of several datasets at ∼40, however. No such coincidence of C/Ba at ∼140 is apparent here, save for Háleyjabunga and Miðfell. However, it could be that Háleyjabunga and Miðfell are unique in sampling a mantle component that does not have a C/Ba ratio of ∼40, and the argument made by Matthews et al. (2017) should be refined to apply only to the depleted upper mantle; Háleyjabunga and Miðfell both have noble gas isotopic ratios that suggest a deep mantle component contributes to their genesis (Breddam et al., 2000; Füri et al., 2010; Mukhopadhyay, 2012). The implication of a mantle component with higher C/Ba is considered in the following sections.

6.5.2. Primordial carbon residing in the Earth

Miller et al. (2019) suggested that the high C/Ba and C/Nb ratios recorded by the Miðfell melt inclusions were evidence for a carbon-rich primitive mantle component. Miðfell is known to sample a mantle component with high ^{3}He/^{4}He (Füri et al., 2010) and ancient Xe and Ne isotopic signatures (Mukhopadhyay, 2012). Háleyjabunga lavas also have elevated ^{3}He/^{4}He (R/R_a = 14.3, Breddam et al., 2000; Füri et al., 2010), the high C/Ba and C/Nb ratios seen in its melt inclusions are therefore consistent with the hypothesis made by Miller et al. (2019). Stapafell and Surtsey have slightly elevated ^{3}He/^{4}He, but their melt inclusions do not have elevated C/Ba or C/Nb; their positions on the global array, however, suggest that their maximum C/Ba and C/Nb ratios are limited by decrepitation (i.e., the eruptions are overall too enriched to have produced inclusions that avoided degassing).

If the high ^{3}He/^{4}He mantle component has a high C/Ba ratio, is the

corollary of its high C/Ba that it has a large carbon budget, as proposed by Miller et al. (2019)? To estimate the carbon content of a mantle component from its C/Ba ratio requires an estimate of its Ba concentration. Unlike for the depleted mantle (e.g., Workman and Hart, 2005), or many enriched mantle components (e.g., Stracke et al., 2003), we lack constraints on the trace element concentrations of the high $^{3}He/^{4}He$ mantle. If the high $^{3}He/^{4}He$ component has similar trace element abundances to the depleted upper mantle (Class and Goldstein, 2005) – and the high C/Ba ratio preserved by inclusions reflect their mantle source – then it must have higher carbon concentrations than the depleted mantle.

An extremely carbon rich mantle component will have profoundly different melting behaviour to a mantle component with $\sim$30 ppmw carbon, a typical estimate for the depleted upper mantle (Hirschmann, 2018); this includes significant quantities of carbonated melt production at great depth (Dasgupta and Hirschmann, 2010). Whilst seismic low-velocity zones, and electrical-conductivity profiles suggest the presence of small quantities of carbonated melt at depth (Dasgupta et al., 2013), there is no evidence for a greater extent of carbonated melt production beneath Iceland than beneath typical mid-ocean ridges. Furthermore, the major element chemistry of Icelandic magmas is well accounted for by silicate-dominated mantle melting (Shorttle and Maclennan, 2011). However, the high $^{3}He/^{4}He$ mantle component need only make up a tiny volume fraction of the Icelandic mantle, if its derivative melts are sufficiently He-rich that they dominate the He-budget of the mixed magma (Porcelli and Elliott, 2008). Carbon enrichment in only the high $^{3}He/^{4}He$ mantle component would have little influence on bulk mantle

properties.

6.5.3. Mantle components with extreme lithophile trace element depletion

A mantle component might have high C/Ba and C/Nb ratios owing to extreme Ba and Nb depletion. The high $^{3}He/^{4}He$ mantle component must have formed during the Earth's differentiation (Porcelli and Elliott, 2008), and might reflect a cumulate formed from a deep magma ocean (Labrosse et al., 2007; Coltice et al., 2011). Trace element parititoning experiments suggest that cumulates dominated by Bridgmanite and Ferropericlase are likely to be extremely trace element depleted (Walter et al., 2004; Corgne et al., 2005). For a cumulate to retain high $^{3}He/^{4}He$ and impart this signature to mixed magmas when melted in the upper mantle, Coltice et al. (2011) showed that the solid-melt partition coefficient for He must be at least 0.01 during magma-ocean crystallisation. Whilst helium behaves more incompatibly than this at low pressures (Parman et al., 2005; Heber et al., 2007), its partitioning behaviour in the lower mantle remains unknown. The requirement for helium to be more compatible in the lower mantle might be relaxed if there is a flux of helium from another reservoir, such as the core (Porcelli and Halliday, 2001), into the depleted cumulates. Incorporation of carbon into such a component is unlikely to occur by carbon partitioning into the silicate phases (Shcheka et al., 2006), but could occur by saturation of a carbon-bearing phase (e.g., Hirschmann, 2012; Armstrong et al., 2019), or by carbon partitioning into a retained metallic iron phase (e.g., Frost et al., 2004; Wade and Wood, 2005).

It is also possible that there is an additional extremely-depleted mantle component, with $^{3}He/^{4}He$ values typical of upper mantle, but elevated

C/Ba and C/Nb. If an extremely depleted component with upper mantle $^3He/^4He$ is present in the Icelandic mantle, analysis of melt inclusions from other extremely trace-element depleted eruptions might be expected to reveal high C/Ba ratios in the absence of high $^3He/^4He$. Both the Heilagsdalsdjall (this study) and Borgarhraun (Hauri et al., 2018) melt inclusion suites are similarly depleted, yet do not contain inclusions with such high C/Ba and C/Nb. For now, we therefore favour the alternative hypothesis, that high C/Ba and C/Nb ratios are associated with the high $^3He/^4He$ component, as it is the most parsimonious explanation for the data. Whether the high $^3He/^4He$ mantle component has high C/Ba and C/Nb ratios by virtue of carbon enrichment or trace element depletion has profound implications for the Earth's carbon budget, and how it has evolved throughout Earth's history.

7. Conclusions

We have leveraged a large new melt inclusion dataset of trace element and carbon concentrations in geochemically diverse Icelandic eruptions, alongside existing suites of melt inclusions, to place new constraints on the interplay of source and process on melt inclusion C/Ba and C/Nb ratios. Though there is a global covariation of C/Ba with enrichment in melt inclusions, this is a result of olivine decrepitation limiting the carbon concentration in melt inclusions. The highest C/Ba and C/Nb ratios seen in inclusions from the most depleted eruptions fall below the decrepitation threshold, potentially preserving the C/Ba and C/Nb ratios of their mantle source. Similarly to melt inclusions from the high $^3He/^4He$ Miðfell eruption (Miller et al., 2019), extremely high C/Ba (>100) and C/Nb (>1000) ratios are seen in inclusions

from the high $^{3}He/^{4}He$ Háleyjabunga eruption. We demonstrate it is unlikely that the high C/Ba and C/Nb ratios are generated by fractionation during melting, or are analytical artefacts. Whilst it is possible that the high C/Ba and C/Nb values are generated by graphite-saturated melting or melt "re-gassing", we suggest they most likely represent high C/Ba and C/Nb ratios in the high $^{3}He/^{4}He$ mantle component. Such high C/Ba and C/Nb values in a mantle component may derive from elevated carbon concentrations (Miller et al., 2019), or by extreme depletion in Ba and Nb inherited from magma-ocean processes. In any case, the high C/Ba and C/Nb ratios are likely to reflect only a small fraction of the Icelandic mantle.

8. Acknowledgements

The authors wish to thank Rob Clarke, Chris Parish, Martin Walker and Ben Winpenny for their assistance with sample preparation, Sébastien Facq and David Neave for their help with operating the Raman instrument, Iris Buisman for her help with the SEM and EPMA measurements, and Richard Hinton for his help with the SIMS analyses. Helen Williams is thanked for commenting on an early version of the manuscript. Callum Reekie and Penny Weiser are thanked for helpful discussions. The text was significantly improved thanks to reviews by Marc Hirschmann, Andreas Stracke, Jonathan Tucker, and two anonymous reviewers. The authors thank Peter Kelemen for lively discussions about mantle carbon.

The SIMS analyses were made at the Natural Environment Research Council Edinburgh Ion-Microprobe Facility under grant numbers IMF579/1015 and IMF616/1016. The authors would like to thank the Isaac Newton Insti-

tute for Mathematical Sciences for its hospitality during the programme 'Melt in the Mantle', which was supported by EPSRC Grant Number EP/K032208/1. SM was supported by a Natural Environment Research Council Studentship NE/L002507/1 and NE/M000427/1. JFR thanks the Leverhulme Trust.

The figures used in this paper were generated with the matplotlib and basemap python packages (Hunter, 2007). Data reduction was performed using the numpy (Oliphant, 2006) and pandas (McKinney, 2010) python packages.

References

Aigner-Torres, M., Blundy, J., Ulmer, P., Pettke, T., 2007. Laser ablation ICPMS study of trace element partitioning between plagioclase and basaltic melts: an experimental approach. Contributions to Mineralogy and Petrology 153 (6), 647–667.

Aiuppa, A., Fischer, T. P., Plank, T., Bani, P., 2019. Co_2 flux emissions from the Earth's most actively degassing volcanoes, 2005–2015. Scientific reports 9 (1), 1–17.

Allison, C. M., Roggensack, K., Clarke, A. B., 2019. H_2O–CO_2 solubility in alkali-rich mafic magmas: new experiments at mid-crustal pressures. Contributions to Mineralogy and Petrology 174 (7), 58.

Anderson, K. R., Poland, M. P., 2017. Abundant carbon in the mantle beneath Hawai'i. Nature Geoscience 10 (9), 704.

Armstrong, K., Frost, D. J., McCammon, C. A., Rubie, D. C., Ballaran,

867 T. B., 2019. Deep magma ocean formation set the oxidation state of Earth's
868 mantle. Science 365 (6456), 903–906.

869 Bali, E., Hartley, M., Halldórsson, S., Gudfinnsson, G., Jakobsson, S., 2018.
870 Melt inclusion constraints on volatile systematics and degassing history of
871 the 2014–2015 Holuhraun eruption, Iceland. Contributions to Mineralogy
872 and Petrology 173 (2), 9.

873 Berry, A. J., Stewart, G. A., O'Neill, H. S. C., Mallmann, G., Mosselmans,
874 J. F. W., 2018. A re-assessment of the oxidation state of iron in MORB
875 glasses. Earth and Planetary Science Letters 483, 114–123.

876 Bézos, A., Humler, E., 2005. The $Fe^{3+}/\Sigma Fe$ ratios of MORB glasses and their
877 implications for mantle melting. Geochimica et Cosmochimica Acta 69 (3),
878 711–725.

879 Boudoire, G., Rizzo, A. L., Di Muro, A., Grassa, F., Liuzzo, M., 2018. Ex-
880 tensive CO_2 degassing in the upper mantle beneath oceanic basaltic vol-
881 canoes: First insights from Piton de la Fournaise volcano (La Réunion
882 Island). Geochimica et Cosmochimica Acta 235, 376–401.

883 Breddam, K., Kurz, M. D., Storey, M., 2000. Mapping out the conduit of the
884 Iceland mantle plume with helium isotopes. Earth and Planetary Science
885 Letters 176 (1), 45–55.

886 Cabral, R. A., Jackson, M. G., Koga, K. T., Rose-Koga, E. F., Hauri, E. H.,
887 Whitehouse, M. J., Price, A. A., Day, J., Shimizu, N., Kelley, K. A.,
888 2014. Volatile cycling of H_2O, CO_2, F, and Cl in the HIMU mantle: A
889 new window provided by melt inclusions from oceanic hot spot lavas at

mangaia, cook islands. Geochemistry, Geophysics, Geosystems 15 (11), 4445–4467.

Cartigny, P., Pineau, F., Aubaud, C., Javoy, M., 2008. Towards a consistent mantle carbon flux estimate: Insights from volatile systematics (H_2O/Ce, δD, CO_2/Nb) in the north atlantic mantle (14°N and 34°N). Earth and Planetary Science Letters 265 (3-4), 672–685.

Class, C., Goldstein, S. L., 2005. Evolution of helium isotopes in the Earth's mantle. Nature 436 (7054), 1107.

Coltice, N., Moreira, M., Hernlund, J., Labrosse, S., 2011. Crystallization of a basal magma ocean recorded by helium and neon. Earth and Planetary Science Letters 308 (1-2), 193–199.

Corgne, A., Liebske, C., Wood, B. J., Rubie, D. C., Frost, D. J., 2005. Silicate perovskite-melt partitioning of trace elements and geochemical signature of a deep perovskitic reservoir. Geochimica et Cosmochimica Acta 69 (2), 485–496.

Cottrell, E., Kelley, K. A., 2011. The oxidation state of Fe in MORB glasses and the oxygen fugacity of the upper mantle. Earth and Planetary Science Letters 305 (3), 270–282.

Cottrell, E., Kelley, K. A., 2013. Redox heterogeneity in mid-ocean ridge basalts as a function of mantle source. Science 340 (6138), 1314–1317.

Dasgupta, R., Hirschmann, M. M., 2010. The deep carbon cycle and melting in earth's interior. Earth and Planetary Science Letters 298 (1-2), 1–13.

912 Dasgupta, R., Mallik, A., Tsuno, K., Withers, A. C., Hirth, G., Hirschmann,
913 M. M., 2013. Carbon-dioxide-rich silicate melt in the Earth's upper mantle.
914 Nature 493 (7431), 211–215.

915 Dixon, J. E., 1997. Degassing of alkalic basalts. American Mineralogist 82 (3-
916 4), 368–378.

917 Dixon, J. E., Stolper, E. M., Holloway, J. R., 1995. An experimental study of
918 water and carbon dioxide solubilities in mid-ocean ridge basaltic liquids.
919 Part I: calibration and solubility models. Journal of Petrology 36 (6), 1607–
920 1631.

921 Duncan, M. S., Dasgupta, R., Tsuno, K., 2017. Experimental determination
922 of CO_2 content at graphite saturation along a natural basalt-peridotite
923 melt join: Implications for the fate of carbon in terrestrial magma oceans.
924 Earth and Planetary Science Letters 466, 115–128.

925 Eguchi, J., Dasgupta, R., 2018a. A CO_2 solubility model for silicate melts
926 from fluid saturation to graphite or diamond saturation. Chemical Geology
927 487, 23–38.

928 Eguchi, J., Dasgupta, R., 2018b. Redox state of the convective mantle from
929 CO_2-trace element systematics of oceanic basalts. Geochemical Perspec-
930 tives Letters 8.

931 Frost, D. J., Liebske, C., Langenhorst, F., McCammon, C. A., Trønnes, R. G.,
932 Rubie, D. C., 2004. Experimental evidence for the existence of iron-rich
933 metal in the Earth's lower mantle. Nature 428 (6981), 409–412.

Füri, E., Hilton, D., Halldórsson, S., Barry, P., Hahm, D., Fischer, T., Grönvold, K., 2010. Apparent decoupling of the he and ne isotope systematics of the Icelandic mantle: The role of He depletion, melt mixing, degassing fractionation and air interaction. Geochimica et Cosmochimica Acta 74 (11), 3307–3332.

Gale, A., Langmuir, C. H., Dalton, C. A., 2014. The global systematics of ocean ridge basalts and their origin. Journal of Petrology 55 (6), 1051–1082.

Hartley, M. E., Maclennan, J., Edmonds, M., Thordarson, T., 2014. Reconstructing the deep CO_2 degassing behaviour of large basaltic fissure eruptions. Earth and Planetary Science Letters 393, 120–131.

Hauri, E. H., Maclennan, J., McKenzie, D., Gronvold, K., Oskarsson, N., Shimizu, N., 2018. CO_2 content beneath northern Iceland and the variability of mantle carbon. Geology 46 (1), 55–58.

Heber, V. S., Brooker, R. A., Kelley, S. P., Wood, B. J., 2007. Crystal–melt partitioning of noble gases (helium, neon, argon, krypton, and xenon) for olivine and clinopyroxene. Geochimica et Cosmochimica Acta 71 (4), 1041–1061.

Hirschmann, M. M., 2012. Magma ocean influence on early atmosphere mass and composition. Earth and Planetary Science Letters 341, 48–57.

Hirschmann, M. M., 2018. Comparative deep earth volatile cycles: The case for C recycling from exosphere/mantle fractionation of major (H_2O, C, N)

volatiles and from H_2O/Ce, CO_2/Ba, and CO_2/Nb exosphere ratios. Earth and Planetary Science Letters.

Hjartarson, Á., Sæmundsson, K., 2014. Geological map of Iceland, bedrock. 1: 600,000. Iceland GeoSurvey, Reykjavík.

Hofmann, A. W., 1997. Mantle geochemistry: the message from oceanic volcanism. Nature 385 (6613), 219–229.

Iacono-Marziano, G., Morizet, Y., Le Trong, E., Gaillard, F., 2012. New experimental data and semi-empirical parameterization of H_2O–CO_2 solubility in mafic melts. Geochimica et Cosmochimica Acta 97, 1–23.

Jackson, D. A., Somers, K. M., 1991. The spectre of 'spurious' correlations. Oecologia 86 (1), 147–151.

Jones, M., Wanless, V., Soule, S., Kurz, M., Mittelstaedt, E., Fornari, D., Curtice, J., Klein, F., Le Roux, V., Brodsky, H., et al., 2019. New constraints on mantle carbon from Mid-Atlantic Ridge popping rocks. Earth and Planetary Science Letters 511, 67–75.

Katz, R. F., Spiegelman, M., Langmuir, C. H., 2003. A new parameterization of hydrous mantle melting. Geochemistry, Geophysics, Geosystems 4 (9).

Kelemen, P. B., Manning, C. E., 2015. Reevaluating carbon fluxes in subduction zones, what goes down, mostly comes up. Proceedings of the National Academy of Sciences, 201507889.

Labrosse, S., Hernlund, J., Coltice, N., 2007. A crystallizing dense magma ocean at the base of the Earth's mantle. Nature 450 (7171), 866–869.

978 Le Voyer, M., Kelley, K., Cottrell, E., Hauri, E., 2017. Heterogeneity in
979 mantle carbon content from CO_2-undersaturated basalts. Nature commu-
980 nications 8, 14062.

981 Lee, C.-T. A., Jiang, H., Dasgupta, R., Torres, M., 2019. A framework
982 for understanding whole-Earth carbon cycling. In: Deep Carbon: Past
983 to Present. Cambridge University Press, pp. 313–357.

984 Maclennan, J., 2008a. Concurrent mixing and cooling of melts under iceland.
985 Journal of Petrology 49 (11), 1931–1953.

986 Maclennan, J., 2008b. Lead isotope variability in olivine-hosted melt inclu-
987 sions from Iceland. Geochimica et Cosmochimica Acta 72 (16), 4159–4176.

988 Maclennan, J., 2017. Bubble formation and decrepitation control the
989 CO_2 content of olivine-hosted melt inclusions. Geochemistry, Geophysics,
990 Geosystems 18 (2), 597–616.

991 Maclennan, J., McKenzie, D., Grönvold, K., Shimizu, N., Eiler, J., Kitchen,
992 N., 2003a. Melt mixing and crystallization under Theistareykir, northeast
993 Iceland. Geochemistry, Geophysics, Geosystems 4 (11).

994 Maclennan, J., McKenzie, D., Hilton, F., Gronvöld, K., Shimizu, N., 2003b.
995 Geochemical variability in a single flow from northern Iceland. Journal of
996 Geophysical Research: Solid Earth 108 (B1), ECV–4.

997 Matthews, S., Shorttle, O., Rudge, J. F., Maclennan, J., 2017. Constraining
998 mantle carbon: CO_2-trace element systematics in basalts and the roles of
999 magma mixing and degassing. Earth and Planetary Science Letters 480,
1000 1–14.

McCammon, C., 2005. The paradox of mantle redox. Science 308 (5723), 807–808.

Métrich, N., Wallace, P. J., 2008. Volatile abundances in basaltic magmas and their degassing paths tracked by melt inclusions. Reviews in mineralogy and geochemistry 69 (1), 363–402.

Métrich, N., Zanon, V., Créon, L., Hildenbrand, A., Moreira, M., Marques, F. O., 2014. Is the 'Azores hotspot' a wetspot? insights from the geochemistry of fluid and melt inclusions in olivine of Pico basalts. Journal of Petrology 55 (2), 377–393.

Michael, P. J., Graham, D. W., 2015. The behavior and concentration of CO_2 in the suboceanic mantle: inferences from undegassed ocean ridge and ocean island basalts. Lithos 236, 338–351.

Miller, W. G., Maclennan, J., Shorttle, O., Gaetani, G. A., Le Roux, V., Klein, F., 2019. Estimating the carbon content of the deep mantle with Icelandic melt inclusions. Earth and Planetary Science Letters 523, 115699.

Moussallam, Y., Longpré, M.-A., McCammon, C., Gomez-Ulla, A., Rose-Koga, E. F., Scaillet, B., Peters, N., Gennaro, E., Paris, R., Oppenheimer, C., 2019. Mantle plumes are oxidised. Earth and Planetary Science Letters 527, 115798.

Mukhopadhyay, S., 2012. Early differentiation and volatile accretion recorded in deep-mantle neon and xenon. Nature 486 (7401), 101–104.

Neave, D. A., Maclennan, J., Edmonds, M., Thordarson, T., 2014. Melt mixing causes negative correlation of trace element enrichment and CO_2

content prior to an Icelandic eruption. Earth and Planetary Science Letters 400, 272–283.

Neave, D. A., Shorttle, O., Oeser, M., Weyer, S., Kobayashi, K., 2018. Mantle-derived trace element variability in olivines and their melt inclusions. Earth and Planetary Science Letters 483, 90–104.

Palme, H., O'Neill, H. S. C., 2003. Cosmochemical estimates of mantle composition. Treatise on geochemistry 2, 568.

Parman, S. W., Kurz, M. D., Hart, S. R., Grove, T. L., 2005. Helium solubility in olivine and implications for high ^{3}he/^{4}he in ocean island basalts. Nature 437 (7062), 1140–1143.

Peate, D. W., Breddam, K., Baker, J. A., Kurz, M. D., Barker, A. K., Prestvik, T., Grassineau, N., Skovgaard, A. C., 2010. Compositional characteristics and spatial distribution of enriched Icelandic mantle components. Journal of Petrology 51 (7), 1447–1475.

Plank, T., Manning, C. E., 2019. Subducting carbon. Nature 574 (7778), 343–352.

Porcelli, D., Elliott, T., 2008. The evolution of helium isotopes in the upper mantle and the generation of isotopic anomalies. Earth Planet. Sci. Lett 269, 175–185.

Porcelli, D., Halliday, A., 2001. The core as a possible source of mantle helium. Earth and Planetary Science Letters 192 (1), 45–56.

1045 Rosenthal, A., Hauri, E., Hirschmann, M., 2015. Experimental determina-
1046 tion of C, F, and H partitioning between mantle minerals and carbonated
1047 basalt, CO_2/Ba and CO_2/Nb systematics of partial melting, and the CO_2
1048 contents of basaltic source regions. Earth and Planetary Science Letters
1049 412, 77–87.

1050 Rudge, J. F., Maclennan, J., Stracke, A., 2013. The geochemical conse-
1051 quences of mixing melts from a heterogeneous mantle. Geochimica et Cos-
1052 mochimica Acta 114, 112–143.

1053 Saal, A. E., Hauri, E. H., Langmuir, C. H., Perfit, M. R., 2002. Vapour un-
1054 dersaturation in primitive mid-ocean-ridge basalt and the volatile content
1055 of earth's upper mantle. Nature 419 (6906), 451.

1056 Sæmundsson, K., Hjartarson, Á., Kaldal, I., Sigurgeirsson, M., Kristinsson,
1057 S., Vikingsson, S., 2012. Geological map of the northern volcanic zone,
1058 Iceland. Northern part 1 (100.000).

1059 Saemundsson, K., Jóhannesson, H., Hjartarson, Á., Kristinsson, S. G., Sig-
1060 urgeirsson, M., 2010. Geological map of southwest Iceland, 1: 100.000.
1061 Iceland GeoSurvey.

1062 Schipper, C. I., Le Voyer, M., Moussallam, Y., White, J. D., Thordarson,
1063 T., Kimura, J.-I., Chang, Q., 2016. Degassing and magma mixing during
1064 the eruption of surtsey volcano (Iceland, 1963–1967): the signatures of a
1065 dynamic and discrete rift propagation event. Bulletin of Volcanology 78 (4),
1066 33.

1067 Shcheka, S. S., Wiedenbeck, M., Frost, D. J., Keppler, H., 2006. Carbon
1068 solubility in mantle minerals. Earth and Planetary Science Letters 245 (3-
1069 4), 730–742.

1070 Shimizu, K., Saal, A. E., Hauri, E. H., Perfit, M. R., Hékinian, R., 2019.
1071 Evaluating the roles of melt-rock interaction and partial degassing on the
1072 CO_2/Ba ratios of MORB: implications for the CO_2 budget in the Earth's
1073 depleted upper mantle. Geochimica et Cosmochimica Acta.

1074 Shimizu, K., Saal, A. E., Myers, C. E., Nagle, A. N., Hauri, E. H., Forsyth,
1075 D. W., Kamenetsky, V. S., Niu, Y., 2016. Two-component mantle melting-
1076 mixing model for the generation of mid-ocean ridge basalts: implications
1077 for the volatile content of the Pacific upper mantle. Geochimica et Cos-
1078 mochimica Acta 176, 44–80.

1079 Shishkina, T. A., Botcharnikov, R. E., Holtz, F., Almeev, R. R., Jazwa,
1080 A. M., Jakubiak, A. A., 2014. Compositional and pressure effects on the
1081 solubility of H_2O and CO_2 in mafic melts. Chemical Geology 388, 112–129.

1082 Shorttle, O., 2015. Geochemical variability in MORB controlled by concur-
1083 rent mixing and crystallisation. Earth and Planetary Science Letters 424,
1084 1–14.

1085 Shorttle, O., Maclennan, J., 2011. Compositional trends of icelandic basalts:
1086 Implications for short–length scale lithological heterogeneity in mantle
1087 plumes. Geochemistry, Geophysics, Geosystems 12 (11).

1088 Shorttle, O., Moussallam, Y., Hartley, M. E., Maclennan, J., Edmonds, M.,
1089 Murton, B. J., 2015. Fe-XANES analyses of Reykjanes Ridge basalts: Im-

plications for oceanic crust's role in the solid Earth oxygen cycle. Earth and Planetary Science Letters 427, 272–285.

Shorttle, O., Rudge, J. F., Maclennan, J., Rubin, K. H., 2016. A statistical description of concurrent mixing and crystallization during MORB differentiation: implications for trace element enrichment. Journal of Petrology 57 (11-12), 2127–2162.

Sides, I., Edmonds, M., Maclennan, J., Swanson, D., Houghton, B., 2014. Eruption style at Kīlauea volcano in Hawai'i linked to primary melt composition. Nature Geoscience 7 (6), 464.

Skovgaard, A. C., Storey, M., Baker, J., Blusztajn, J., Hart, S. R., 2001. Osmium–oxygen isotopic evidence for a recycled and strongly depleted component in the Iceland mantle plume. Earth and Planetary Science Letters 194 (1), 259–275.

Sobolev, A., 1996. Melt inclusions in minerals as a source of principle petrological information. Petrology 4 (3), 209–220.

Sobolev, A., Shimizu, N., 1993. Ultra-depleted primary melt included in an olivine from the mid-atlantic ridge. Nature 363 (6425), 151.

Stolper, E., Holloway, J. R., 1988. Experimental determination of the solubility of carbon dioxide in molten basalt at low pressure. Earth and Planetary Science Letters 87 (4), 397–408.

Stracke, A., Bizimis, M., Salters, V. J., 2003. Recycling oceanic crust: Quantitative constraints. Geochemistry, Geophysics, Geosystems 4 (3).

1112 Stracke, A., Hofmann, A. W., Hart, S. R., 2005. FOZO, HIMU, and the rest
1113 of the mantle zoo. Geochemistry, Geophysics, Geosystems 6 (5).

1114 Thirlwall, M., Gee, M., Taylor, R., Murton, B., 2004. Mantle components
1115 in iceland and adjacent ridges investigated using double-spike Pb isotope
1116 ratios. Geochimica et Cosmochimica Acta 68 (2), 361–386.

1117 Trull, T., Nadeau, S., Pineau, F., Polve, M., Javoy, M., 1993. C-He system-
1118 atics in hotspot xenoliths: Implications for mantle carbon contents and
1119 carbon recycling. Earth and Planetary Science Letters 118 (1-4), 43–64.

1120 Tucker, J. M., Hauri, E. H., Pietruszka, A. J., Garcia, M. O., Marske, J. P.,
1121 Trusdell, F. A., 2019. A high carbon content of the Hawaiian mantle
1122 from olivine-hosted melt inclusions. Geochimica et Cosmochimica Acta
1123 254, 156–172.

1124 Tucker, J. M., Mukhopadhyay, S., Gonnermann, H. M., 2018. Reconstruct-
1125 ing mantle carbon and noble gas contents from degassed mid-ocean ridge
1126 basalts. Earth and Planetary Science Letters 496, 108–119.

1127 Wade, J., Wood, B., 2005. Core formation and the oxidation state of the
1128 Earth. Earth and Planetary Science Letters 236 (1-2), 78–95.

1129 Walter, M., Nakamura, E., Trønnes, R., Frost, D., 2004. Experimental con-
1130 straints on crystallization differentiation in a deep magma ocean. Geochim-
1131 ica et Cosmochimica Acta 68 (20), 4267–4284.

1132 Wanamaker, B., Wong, T.-F., Evans, B., 1990. Decrepitation and crack heal-
1133 ing of fluid inclusions in San Carlos olivine. Journal of Geophysical Re-
1134 search: Solid Earth 95 (B10), 15623–15641.

Wanless, V., Behn, M., Shaw, A., Plank, T., 2014. Variations in melting dynamics and mantle compositions along the Eastern Volcanic Zone of the Gakkel Ridge: insights from olivine-hosted melt inclusions. Contributions to Mineralogy and Petrology 167 (5), 1005.

Wanless, V. D., Shaw, A. M., 2012. Lower crustal crystallization and melt evolution at mid-ocean ridges. Nature Geoscience 5 (9), 651.

Wanless, V. D., Shaw, A. M., Behn, M. D., Soule, S. A., Escartin, J., Hamelin, C., 2015. Magmatic plumbing at Lucky Strike volcano based on olivine-hosted melt inclusion compositions. Geochemistry, Geophysics, Geosystems 16 (1), 126–147.

White, W. M., 2015. Isotopes, DUPAL, LLSVPs, and anekantavada. Chemical Geology 419, 10–28.

Workman, R. K., Hart, S. R., 2005. Major and trace element composition of the depleted MORB mantle (DMM). Earth and Planetary Science Letters 231 (1), 53–72.

Appendix A. Graphite Saturated Melting

In the main text we describe results of extending the degassing and mixing calculations of Matthews et al. (2017) to graphite-present melting. Rudge et al. (2013) and Matthews et al. (2017) provide a thorough description of the model and how it applies to magmatic carbon concentrations. Here we set out how we calculate the carbon concentrations of melts in equilibrium with graphite.

We calculate the carbon content of a melt at graphite saturation using the formulation of Duncan et al. (2017), which depends on fO_2 and magma composition. Once graphite is exhausted, we assume that carbon is entirely depleted from the solid residue. To maintain consistency with other trace elements, which we model as melting continuously, we allow for carbon remaining in melts within the residual porosity, with a growing degree of dilution and assuming perfectly incompatible behaviour.

For a single melting increment of dF_n with a residual porosity of ϕ:

$$C_n = \frac{\phi - dF_n}{\phi} C_{n-1} \tag{A.1}$$

where C_n and $C_(n-1)$ are the carbon concentrations in the residual porosity after, and before the nth melting increment, respectively. This can be applied recursively to yield:

$$C_n = \left[\frac{\phi - dF_n}{\phi}\right] \left[\frac{\phi - dF_{n-1}}{\phi}\right] \cdots \left[\frac{\phi - dF_1}{\phi}\right] C_0 \tag{A.2}$$

$$C_n = \frac{C_0}{\phi^n} \prod_{i=0}^{n-1} \phi - dF_{n-i} \tag{A.3}$$

where C_0 is the carbon concentration in the melt at the point of graphite exhaustion. Setting $dF_{n+1} = dF_n = dF$,

$$C_n = C_0 \left(1 - \frac{dF}{\phi}\right)^n \tag{A.4}$$

and since:

$$dF = \frac{\Delta F}{n} \tag{A.5}$$

where $\Delta F = F - F_{\text{graphite-exhaustion}}$, the concentration at a given ΔF may be written:

$$C\left(\Delta F\right) = C_0 \left(1 - \frac{\Delta F}{\phi n}\right)^n \tag{A.6}$$

in the limit $dF \to 0$ and $n \to \infty$:

$$C\left(\Delta F\right) = C_0 e^{-\frac{\Delta F}{\phi}} \tag{A.7}$$

Examples of these calculations for variable fO_2, are shown in Figure 8.